Science

AAAS

Element-Resolved Corrosion Analysis of Stainless-Type Glass-Forming Steels

M. J. Duarte *et al.*

Science **341**, 372 (2013);
DOI: 10.1126/science.1230081

suggest that quantum effects are crucial (42), because classical turbulence has an inverse cascade in (2+1) dimensions, whereas quantum turbulence—at least in the systems and regimes we have studied—gives a direct cascade. Furthermore, as discussed earlier, the average vortex spacing in our system (~10) falls inside the inertial range (2, 16). Because vortex spacing provides the characteristic length scale at which quantum effects are important, the Kolmogorov scaling observed here would appear to be tightly intertwined with the quantum nature of the fluid. We note that the argument for Kolmogorov scaling only assumes the existence of an inertial range of k values in which the only scale in the system is the overall rate of dissipation, $\mathcal{E}$. This assumption by itself does not require the fluid to be classical or quantum, so the Kolmogorov scaling could well arise from the quantum phenomena seen in our simulations.

Many aspects of superfluid turbulent flow await further investigation, including a better understanding of the physics of vortex drag and annihilation, the dependence of the turbulent phase on parameters such as the mean vortex density, and the physics governing the IR end of the inertial range. Studies of other observables of the superfluid flow, such as velocity statistics, have yielded tantalizing differences between classical and quantum turbulence (43, 44). Attempts to derive the Kolmogorov scaling directly from the holographic dual may also be worthwhile.

Because normal fluids in two spatial dimensions typically experience an inverse cascade, it will be of interest to see how the system behaves depending on the relative weights of the normal and superfluid components. For this purpose, one must go beyond the probe limit we have used here, so as to allow the superfluid flow to interact with the normal fluid component. In the dual gravitational description, this would require inclusion of the back-reaction of the gauge field A_M and scalar field Φ on the bulk geometry, and hence would require the use of numerical relativity to determine the evolution of the system.

many-body systems with which we can explore the space of what is possible, and possibly generic, in such strongly interacting systems. In the longer term, we aim to build realistic models using these holographic tools. Precisely how robust or transferable the present results are to real-world systems remains an open question.

References and Notes

1. R. Feynman, *Prog. Low Temp. Phys.* **1**, 17–53 (1955).
2. W. F. Vinen, *Proc. R. Soc. A* **240**, 114–127 (1957).
3. W. F. Vinen, *Proc. R. Soc. A* **240**, 128–143 (1957).
4. W. F. Vinen, *Proc. R. Soc. A* **242**, 489–515 (1957).
5. W. F. Vinen, J. J. Niemela, *J. Low Temp. Phys.* **128**, 167–231 (2002).
6. M. S. Paoletti, D. P. Lathrop, *Annu. Rev. Condens. Matter Phys.* **2**, 213–234 (2011).
7. M. Tsubota, M. Kobayashi, H. Takeuchi, *Phys. Rep.* **522**, 191–238 (2013).
8. J. M. Maldacena, *Adv. Theor. Math. Phys.* **2**, 231 (1998).
9. S. Gubser, I. R. Klebanov, A. M. Polyakov, *Phys. Lett. B* **428**, 105–114 (1998).
10. E. Witten, *Adv. Theor. Math. Phys.* **2**, 253 (1998).
11. S. A. Hartnoll, *Class. Quantum Gravity* **26**, 224002 (2009).
12. C. P. Herzog, *J. Phys. A* **42**, 343001 (2009).
13. J. McGreevy, *Adv. High Energy Phys.* **2010**, 723105 (2010).
14. J. Casalderrey-Solana, H. Liu, D. Mateos, K. Rajagopal, U. A. Wiedemann, http://arxiv.org/abs/1101.0618 (2011).
15. A. Adams, L. D. Carr, T. Schäfer, P. Steinberg, J. E. Thomas, *N. J. Phys.* **14**, 115009 (2012).
16. Holography, for our present purposes, provides a set of tractable toy models of strongly interacting quantum

17. J. Maurer, P. Tabeling, *Europhys. Lett.* **43**, 29–34 (1998).
18. M. R. Smith, R. J. Donnelly, N. Goldenfeld, W. F. Vinen, *Phys. Rev. Lett.* **71**, 2583–2586 (1993).
19. S. R. Stalp, L. Skrbek, R. J. Donnelly, *Phys. Rev. Lett.* **82**, 4831–4834 (1999).
20. E. A. L. Henn, J. A. Seman, G. Roati, K. M. F. Magalhães, V. S. Bagnato, *Phys. Rev. Lett.* **103**, 045301 (2009).
21. J. A. Seman et al., *J. Phys. Conf. Ser.* **264**, 012004 (2011).
22. C. Nore, M. Abid, M. E. Brachet, *Phys. Rev. Lett.* **78**, 3896–3899 (1997).
23. T. Araki, M. Tsubota, S. K. Nemirovskii, *Phys. Rev. Lett.* **89**, 145301 (2002).
24. M. Kobayashi, M. Tsubota, *Phys. Rev. Lett.* **94**, 065302 (2005).
25. N. G. Parker, C. S. Adams, *Phys. Rev. Lett.* **95**, 145301 (2005).
26. T.-L. Horng, C.-H. Hsueh, S.-W. Su, Y.-M. Kao, S.-C. Gou, *Phys. Rev. A* **80**, 023618 (2009).
27. R. Numasato, M. Tsubota, *J. Low Temp. Phys.* **158**, 415–421 (2010).
28. R. Numasato, M. Tsubota, V. S. L'vov, *Phys. Rev. A* **81**, 063630 (2010).
29. M. T. Reeves, T. P. Billam, B. P. Anderson, A. S. Bradley, *Phys. Rev. Lett.* **110**, 104501 (2013).
30. We label boundary indices by μ, ν, … and bulk indices by M, N, …, with $A_M = (A_\mu, A_z)$.
31. This gravitational system is dual to a conformal field theory; however, conformal symmetry is broken by both the chemical potential and the temperature, so the conformal symmetry plays no role in what follows.
32. S. S. Gubser, *Phys. Rev. D* **78**, 065034 (2008).
33. S. A. Hartnoll, C. P. Herzog, G. T. Horowitz, *Phys. Rev. Lett.* **101**, 031601 (2008).
34. F. Denef, S. A. Hartnoll, *Phys. Rev. D* **79**, 126008 (2009).
35. S. S. Gubser, C. P. Herzog, S. S. Pufu, T. Tesileanu, *Phys. Rev. Lett.* **103**, 141601 (2009).
36. T. Albash, C. V. Johnson, *Phys. Rev. D* **80**, 126009 (2009).
37. M. Montull, A. Pomarol, P. J. Silva, *Phys. Rev. Lett.* **103**, 091601 (2009).
38. V. Keränen, E. Keski-Vakkuri, S. Nowling, K. Yogendran, *Phys. Rev. D* **81**, 126012 (2010).
39. B. V. Svistunov, *Phys. Rev. B* **52**, 3647–3653 (1995).
40. Because different initial conditions lead to qualitatively similar late-time behaviors, we focus for definiteness on a typical example. Images and videos from these simulations are available at http://turbulent.lns.mit.edu/Superfluid.
41. As we discuss below, the winding number $W = \pm 6$ vortices rapidly decay into six $W = \pm 1$ vortices. Therefore, by adjusting the lattice constant and initial winding number, these initial conditions allow us to control the initial density of $W = \pm 1$ vortices.
42. Although our 3D gravitational calculations have been purely classical, the 2D liquid captured by these calculations is a strongly interacting quantum superfluid; the fact that the dynamics of this quantum liquid are captured by classical geometric quantities is an example of the power of the holographic description.
43. M. S. Paoletti, M. E. Fisher, K. R. Sreenivasan, D. P. Lathrop, *Phys. Rev. Lett.* **101**, 154501 (2008).
44. A. C. White, C. F. Barenghi, N. P. Proukakis, A. J. Youd, D. H. Wacks, *Phys. Rev.* **104**, 075301 (2010).

Element-Resolved Corrosion Analysis of Stainless-Type Glass-Forming Steels

M. J. Duarte,[1,2,3,4]*† J. Klemm,[1]† S. O. Klemm,[1] K. J. J. Mayrhofer,[1] M. Stratmann,[1] S. Borodin,[1] A. H. Romero,[2,5]‡ M. Madinehei,[3] D. Crespo,[3] J. Serrano,[6] S. S. A. Gerstl,[4]§ P. P. Choi,[4] D. Raabe,[4] F. U. Renner[1]*||

Ultrathin passive films effectively prevent the chemical attack of stainless steel grades in corrosive environments; their stability depends on the interplay between structure and chemistry of the constituents iron, chromium, and molybdenum (Fe-Cr-Mo). Carbon (C), and eventually boron (B), are also important constituents of steels, although in small quantities. In particular, nanoscale inhomogeneities along the surface can have an impact on material failure but are still poorly understood. Addressing a stainless-type glass-forming $Fe_{50}Cr_{15}Mo_{14}C_{15}B_6$ alloy and using a combination of complementary high-resolution analytical techniques, we relate near-atomistic insights into increasingly inhomogeneous nanostructures with time- and element-resolved dissolution behavior. The progressive elemental partitioning on the nanoscale determines the degree of passivation. A detrimental transition from Cr-controlled passivity to Mo-controlled breakdown is dissected atom by atom, demonstrating the importance of nanoscale knowledge for understanding corrosion.

The environmental degradation of metals by chemical reactions in humid atmospheres or electrolytes results in substantial worldwide annual losses. In applications where corrosion is a critical factor, typically corrosion-resistant polycrystalline Ni-based materials or relatively inexpensive Fe-based steels are employed. In these stainless materials, Cr plays a vital role

in establishing protective passive oxide films of a few atomic layers (*1–3*), which show improved stability by combination with Mo (*4, 5*). Glassy alloys, including amorphous steels, have gained attention, in part due to their extraordinary corrosion and pitting resistance at comparatively low Cr contents (*6–9*). Additionally, an improved mastering of production (*10*) opens promising applications ranging from structural gadgets to biocompatible implant materials (*11–13*). Moreover, the chemical and structural homogeneity of amorphous steel alloys have been recognized as an important asset for addressing fundamentally the influence of alloying elements on their macroscopic behavior such as corrosion (*7, 14, 15*). The metastable glassy structure can be devitrified by gentle annealing (*16*), which enables well-defined intermediate states of nanoscale elemental inhomogeneity. Although inhomogeneities exist on the nanoscale, the annealed structures are homogeneous on the macro scale. Microscopic insights of bulk material can thus be related to macroscopic performance.

Addressing the nanoscale characteristics of passive films of complex stainless steels remains a challenge. Considerable progress in understanding the laterally averaged structure and chemistry of the ultrathin passive films has been achieved by surface analysis techniques (*6, 17, 18*). Despite their importance, however, the influence of nanoscale inhomogeneities on the film reactions such as crystallographic defects, small-scale inclusions, precipitates, grain boundaries, or simple chemical variations along surfaces remains largely unresolved and is still key for advancing modern materials development and corrosion research (*19–21*). The passive films effectively change or block the dissolution of metallic materials in their specific environment. A sensitive multi-elemental online detection of dissolved species during their build-up or steady-state regime, together with a finely resolved knowledge of the underlying substrate, makes this effect discernible and permits insight into the fundamental mechanisms of passivation.

We provide a high-resolution near-atomistic view on the relation between bulk and surface microstructure and time-resolved corrosion performance of the stainless-type amorphous and nanocrystalline alloy $Fe_{50}Cr_{15}Mo_{14}C_{15}B_6$ (*22*). Amorphous ribbons were prepared by melt spinning and crystallized by thermal annealing at the selected temperatures for 20 min. The glass transition ($T_g = 550°C$), the onset of the first and second crystallization ($T_{x1} = 602°C$, $T_{x2} = 641°C$), and the melting temperatures ($T_m = 1112°C$) of the amorphous alloy were obtained by differential scanning calorimetry and serve as an indicator of the structural transformations within the alloy.

Atom probe tomography (APT) (*23*) reconstructions are presented in Fig. 1A (and figs. S1 and S2). Fe, Cr, and Mo are presented in green,

blue, and red colors, respectively. Boron and carbon were omitted here for clarity. The lower images correspond to 2- to 5-nm slices from the reconstructions, elucidating the nanoscale partitioning. Isoconcentration surfaces of Cr and Mo are plotted to highlight regions of highest chemical gradients. The average compositions of the different regions are listed in Table 1. The as-quenched ribbons show the broad diffuse x-ray peaks (Fig. 1B) characteristic of an amorphous structure, whereas a uniform elemental distribution by APT confirms their chemical homogeneity. At 620°C, Cr-rich regions of 12-nm average size are formed by elemental redistribution (Fig. 1A). Correlated analyses between x-ray diffraction (XRD) and transmission electron microscopy (TEM) indicate the presence of the carbide phase
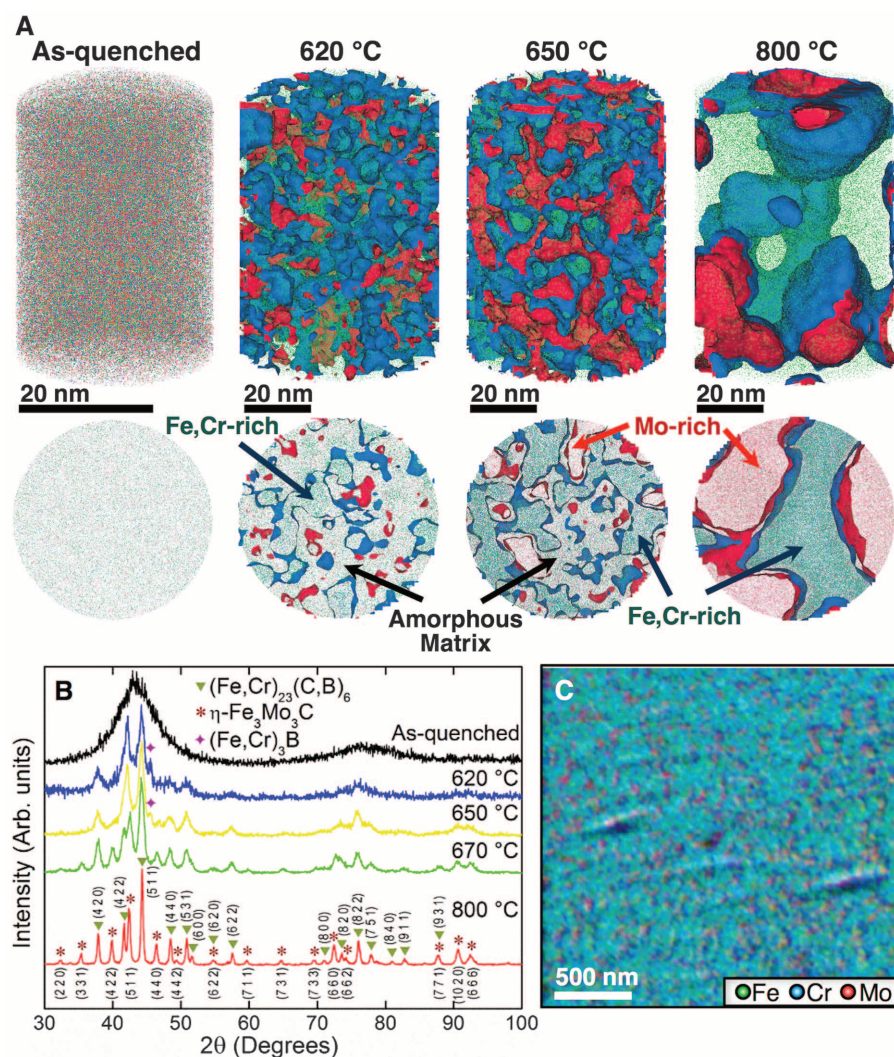
[1]Department of Interface Chemistry and Surface Engineering, Max-Planck Institut für Eisenforschung GmbH, 40237 Düsseldorf, Germany. [2]Departamento de Materiales, Centro de Investigación y de Estudios Avanzados, Instituto Politécnico Nacional (CINVESTAV-IPN), 76230 Queretaro, Mexico. [3]Department de Fisica Aplicada, Universitat Politècnica de Catalunya, 08860 Castelldefels, Spain. [4]Department of Microstructure Physics and Alloy Design, Max-Planck Institut für Eisenforschung GmbH, 40237 Düsseldorf, Germany. [5]Max-Planck Institut für Mikrostrukturphysik, 06120 Halle, Germany. [6]Institució Catalana de Recerca i Estudis Avançats (ICREA), Universitat Politècnica de Catalunya, 08860 Castelldefels, Spain.

*Corresponding author. E-mail: j.duarte@mpie.de (M.J.D.); frank.renner@uhasselt.be (F.U.R.)

†These authors contributed equally to this work.

‡Present address: Physics Department, West Virginia University, Morgantown, WV 26506–6315, USA.

§Present address: Electron Microscopy of Eidgenössische Technische Hochschule Zurich (EMEZ), 8093 Zurich, Switzerland.

‖Present address: Instituut Voor Materiaalonderzoek, Universiteit Hasselt, 3590 Diepenbeek, Belgium.

Fig. 1. Microstructure and surface analysis. (**A**) APT reconstructions showing the distribution of the metallic elements (Fe, green; Cr, blue; Mo, red) in the as-quenched, partially and fully crystallized alloys. Isoconcentration surfaces of 22 atomic % Mo in red and 16 atomic % Cr in blue highlight three different regions in the samples annealed for 20 min at 620° and 650°C. Thirty-two atomic % Mo and 15 atomic % Cr isoconcentration surfaces are plotted for the crystallized alloy (60 min at 800°C). Lower images are 2- to 5-nm thick virtual slices of the respective reconstructions revealing the nanoscale partitioning characteristics. (**B**) XRD plots indicating the formation of the different phases. (**C**) Overlap of the individual Fe, Cr, and Mo SAEM maps after crystallization at 800°C.

$M_{23}(C,B)_6$ (with M=Fe,Cr,Mo). Molybdenum atoms segregate from these carbides to the amorphous matrix, forming additional regions enriched in Mo (red areas at 620°C) until a crystalline η-Fe_3Mo_3C phase is observed at 650°C. M_3B and a solid solution τFe-Cr-Mo are present as intermediate phases only in the 620° to 650°C temperature range. The fully crystallized sample (at 800°C) shows Mo-rich and Cr-rich phases of up to 50 nm in size (see also fig. S3). The chemical composition in the respective regions becomes thermodynamically stable with increasingly sharp boundaries. Most important, for our passivation studies, a percolation of both crystalline phases throughout the fully crystallized sample is observed.

Freshly sputtered starting surfaces were used to ensure reproducibility of the electrochemical measurements and surface analysis. Bombardment with Ar ions essentially cleaned the surfaces from contaminations or any reaction layers formed during annealing (fig. S4). The elemental distribution of the fresh surface of the fully nanocrystalline sample in the scanning Auger EM (SAEM) map (overlaid map in Fig. 1C) closely corresponds to the distribution displayed in the APT slice in Fig. 1A. Although some sputter ripples emerge in the surface morphology, sputtering is thus able to produce an almost ideal cut of the bulk material, and the detailed bulk microstructure information is maintained at the surface.

Micro-electrochemical corrosion tests enabled a large number of tests on one sample and showed an excellent reproducibility (24). Depending on the thermal history, the electrochemical corrosion behavior reveals a transition from an extended passive state limited by transpassive Cr dissolution to an early breakdown governed by transpassive Mo dissolution (Fig. 2A in 0.1 M H_2SO_4 and fig. S5 in 0.1 M HCl). The curves obtained are located between the reference behavior of pure Mo and pure Cr. In region (a) of Fig. 2A, oxidizing positive currents indicate the release of metal ions. For the alloys crystallized above 670°C, the steep increase in current is linked to strong metal dissolution. Below 650°C, the annealed and the pristine amorphous alloys show a transition into a further low-current passive region (b). The initial peak indicates the transition of a native oxide film, which is unstable in the electrolyte, toward this passive state. In region (c), the passive film breaks down about 100 mV earlier than the transpassive Cr dissolution of the pure Cr foil. Interestingly, the partially nanocrystalline samples below 620°C show only a moderately larger passive current density. The transition peak (a) is more pronounced, and the final breakdown occurs at the same potential compared with the amorphous alloy. The transition in breakdown behavior appears between 620° and 670°C. The fully nanocrystalline sample (800°C) closely resembles the behavior of pure Mo but is about 100 mV more stable. APT analyses indicate 6 to 7 atomic percent (atomic %) of Cr in the respective Mo-rich phase. In particular, for com-

plex multi-element materials the total current does not reveal sufficient information on the involved elements.

Of particular interest for corrosion performance are the individual elemental contribution and the effectiveness of the passivating elements Cr and Mo (7, 25, 26). Element-resolved dissolution data were measured online using a scanning flow cell (SFC) with an inductively coupled plasma mass spectrometer (ICP-MS) (27) and are illustrated for three selected states in Fig. 2, B to
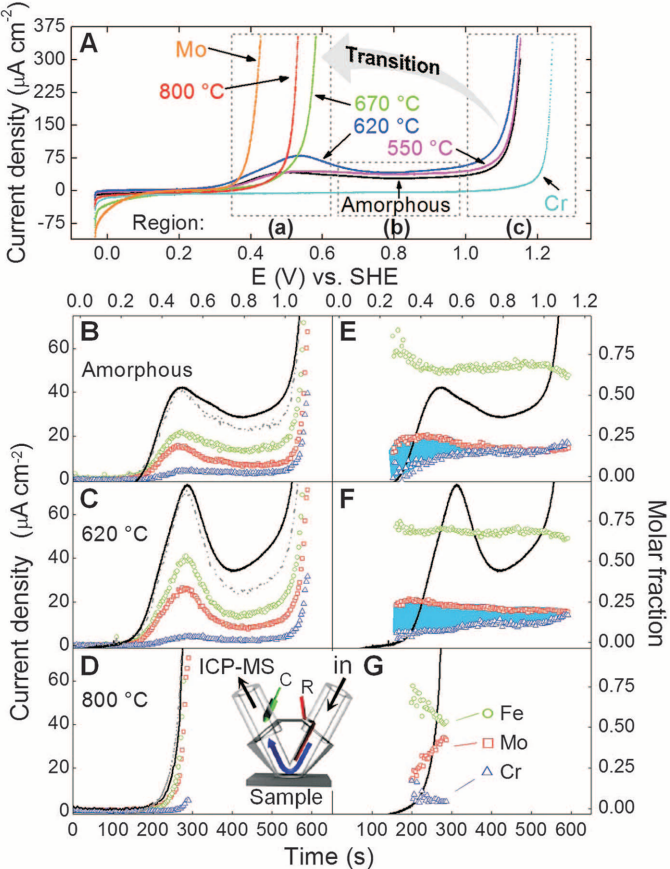
G. The measured concentrations were converted into current densities by application of Faraday's law (27–29). The sum of all three elemental dissolution current densities, $i_{Diss,Me}$ with Me = Fe, Cr, Mo (gray dashed lines in Fig. 2, B to D), shows good agreement with the measured current density i_m for all three samples. Visible deviations reflect the growth of the 1- to 2-nm passive film and dissolution of carbon and boron. Compared with the bulk composition, the element-specific dissolution stoichiometry (molar fractions)

Table 1. Representative concentration of the metallic components (in atomic %) in the different regions determined by APT and SFC-ICP-MS.

				APT								
Alloy	**Am**	**550°C**	**620°C**		**650°C**			**670°C**		**800°C**	
Zone (Fig.1A)			Cr-rich	Matrix	Cr-rich	Mo-rich	Matrix	Cr-rich	Mo-rich	Cr-rich	Mo-rich
% Fe	59	59	61	58	65	44	59	65	44	65	42
% Cr	19	18	26	19	23	9	19	23	8	22	7
% Mo	22	23	13	23	12	47	22	12	48	13	51
				ICP − MS							
Alloy	**Amorphous (Am)**			**550°C**			**620°C**			**670°C**	**800°C**
Region (Fig. 2)	a	b	c	a	b	c	a	b	c	a	a
% Fe	65	68	63	68	72	63	71	70	64	56	53
% Cr	13	16	20	11	14	19	7	10	17	7	4
% Mo	22	16	17	21	14	18	22	20	19	37	43

Fig. 2. Electrochemical behavior and element-resolved online analysis. (**A**) Potentiodynamic polarization curves in 0.1 M H_2SO_4 (2 mV/s in the positive direction) of amorphous, partially (620°C) and fully nanocrystalline (800°C) $Fe_{50}Cr_{15}Mo_{14}C_{15}B_6$ together with pure Cr and Mo. (**B** to **D**) Online ICP-MS dissolution profiles converted into dissolution current densities ($i_{Diss,Me}$, Me = Fe, Cr, Mo with green, blue, and red symbols, respectively, and $i_{Diss,total}$ = sum of individual $i_{Diss,Me}$, gray dashed line) for the (B) amorphous, (C) partially nanocrystalline, and (D) fully nanocrystalline alloy. Potential sweep data, i_m, as black line. (**E** to **G**) Dissolution stoichiometry expressed as molar fractions of Fe, Cr, and Mo, for the (E) amorphous, (F) partially nanocrystalline, and (G) fully nanocrystalline alloys. The difference between Mo and Cr dissolution is highlighted in blue. The inset shows a schematic figure of the SFC-ICP-MS.

reveals significant changes at different times and potentials (Fig. 2, E to G). The main species dissolved in the lower range of potentials up to 700 mV for the amorphous sample is Fe, with substoichiometric dissolution of Cr. The time-resolved enrichment of Cr on the surface can thus directly be followed. At higher potentials in the passive range, both Mo and Cr dissolve in equivalent ratios reflecting the substrate composition. A higher contribution of Fe and Mo is observed in the sample annealed at 620°C. Cr dissolves then stoichiometrically only at the breakdown. The formation of Cr-rich crystals, and consequently Cr-depleted regions, leads to the increase in the current density. Formation of passive layers is accompanied by a large etching effect that is enhanced by the codissolution of Cr, because the necessary accumulation of Cr is delayed. The inhomogeneous substrates revealed two time scales, one initial strong dissolution peak and a slower process to reach the final steady state. A relatively thick layer of the amorphous and the partially crystalline surface is removed (about 20 and 30 nm in average, respectively), as can be deduced from the elemental dissolution data. A thicker and significantly Cr-enriched passive film is thus formed after immersion in the electrolyte. Independent x-ray photoelectron spectroscopy (XPS) measurements (fig. S6) confirm the increase in film thickness to about 4 nm and reveal the thickness and composition of the respective passive oxide films to closely resemble the reported films on binary Fe-Cr model alloys or stainless steels. In contrast, the fully nanocrystalline alloy (800°C) shows an increasingly strong contribution of Mo, with Cr being distinctly minor. The dissolution stoichiometry is thus quickly dominated by the Mo-rich phase, and the chemical stability of the system is compromised with the formation of the percolating Cr-depleted structure. The individual amounts of metals dissolved in the specific potential regions are given in Table 1. The ratio of Fe and Mo measured by APT in the Mo-rich phase agrees very well with the dissolution of the nanocrystalline material during the potential sweeps. This supports that the electrochemical behavior in the crystallized alloys is indeed dominated by the Mo-

rich and severely Cr-depleted phase, which begins to corrode at low potentials. In parallel to the growth of the adapted passive film, the associated selective etching results in a severe surface roughening on the nanometer length-scale of the formed chemical inhomogeneities. Figure 3A shows an atomic force microscopy (AFM) image of the surface morphology after initial corrosion of the partially crystalline state (annealed at 620°C). The final transpassive breakdown of the layer is here not compromised by the developing defects in the surface morphology and the partial crystallization. The completely amorphous sample shows no difference in roughness before and after formation of the passive layer, confirming its homogeneous nature. Only at high temperatures does a more pronounced chemical partitioning with a fully developed phase percolation cause the mechanism and the breakdown potential to change.

Continuous selective dissolution can be sustained as shown in Fig. 3, B and C, for the alloy crystallized at 800°C. TEM confirms the homogeneity of the sample on larger length scales than APT and the dissolution of a percolating Mo-rich phase. Chemical partitioning is independently confirmed in the high-angle annular dark field (HAADF) scanning TEM (STEM) image as variations in contrast (Fig. 3B), in addition to local energy dispersive x-ray (EDX) analysis (Fig. 3C). The resulting mesoporous Cr-rich carbide is chemically very stable and may be useful for different applications.

The complexity of most applied materials often precludes a thorough understanding of the macroscopic behavior, including corrosion. Here, we followed the role and fate of the individual elements during the corrosion of a complex multi-element material. First, the three-dimensional near-atomistic chemical distribution revealed by APT discloses the increasing Cr partitioning of the alloy at different temperatures, which is essential for understanding the breakdown of effectiveness of passivation. The Cr depletion first occurs homogeneously throughout the remaining matrix—that is, no sensitization is observed. The Cr-depleted η-Fe_3Mo_3C phase does not form surrounding, nor always attached to, the Cr-enriched crystallites. Approaching the fully crystallized state at
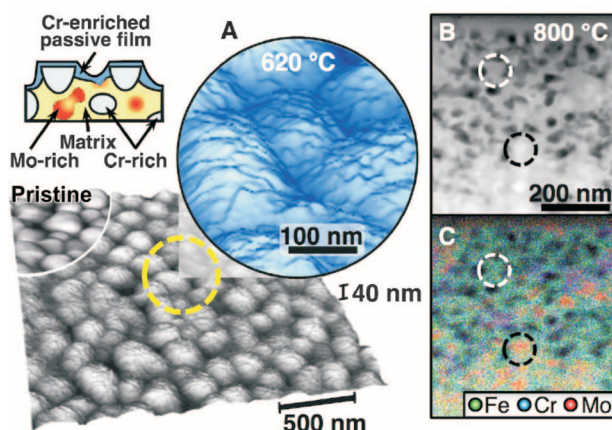
700° to 800°C, the η-phase percolates throughout the alloy and the passivation mechanism completely fails.

The sensitive and directly linked online ICP-MS dissolution analysis is a second major point. Alloying elements can considerably influence the behavior of materials; they can block dissolution sites or catalyze reactions, either beneficial or detrimental. Cr is codissolved at all stages in different ratios. Enrichment of Cr on the surface drives passivation and is, according to our time- and element-resolved data, much slower for the partially crystalline sample compared with the completely amorphous one. At the same time, major surface etching (10 to 30 nm) takes place, which results in a higher surface roughness but may also help to overgrow a structurally inhomogeneous substrate. Nevertheless, the finally established passive state exhibits a slightly higher passive current compared with the amorphous state. The transpassive breakdown process occurs at lower potentials for the analyzed alloys compared with pure Cr, thus indicating a further codissolution effect of the alloying elements and marking a change in mechanism during the potential ramp. After a steady state has been reached for a passive film, the samples dissolve with bulk stoichiometry, whereas the early breakdown of the fully nanocrystalline state is associated with a very high Mo dissolution.

As a general remark, the structure of passive films on stainless steels has been recognized as an amorphous-crystalline composite (30). Granted, the rigorous nanometer-scale lateral chemical composition of any ultrathin passive film has not been resolved so far. Amorphous steels show a low threshold to develop a protective film of 4 to 5% Cr (31) compared with 12 to 13% Cr in crystalline stainless steel alloys (32). The origin of this lower threshold remains disputed and was attributed either to the amorphous substrate facilitating an entirely amorphous passive film structure or to a more homogeneous Cr distribution. Although element-resolved solution analysis marks an enormous step for our understanding, more detailed insight into the passive film itself will be necessary to resolve the issue completely.

Finally, beyond the particular amorphous and nanocrystalline alloy presented here, interesting parallels to commercial polycrystalline stainless steels can be drawn. The passive films of both are of the same nature—that is, they have the same thickness and average composition. High-performance austenitic stainless steel grades such as American Iron and Steel Institute (AISI) types 316L, 904L, or 654 SMO contain a relatively high amount of Mo (2 to 7 weight percent) and are employed where corrosion behavior is critical. Passive films are not static but adapt to changes in the environment and are partially able to heal defective regions such as local variations in Cr, weld precipitations, tiny impurity phases, or sensitized grain boundaries. We showed how a passivation scheme for amorphous and nanocrystalline steels reacts to local chemical

Fig. 3. Surface analysis and cross section after galvanostatic corrosion. (**A**) AFM images and sketch of a rough surface after corrosion of a sample annealed at 620°C for 20 min. (**B**) HAADF-STEM micrograph of the fully crystallized alloy after polarization for 4000 s and (**C**) corresponding EDX map showing the Mo, Fe, and Cr distributions in the porous layer and the bulk. Mo-rich and Cr-rich areas are bordered by black and white dashed circles, respectively.

variations down to the nanometer scale. Herein lies the benefit in studying these types of steels to understand specific aspects of real-world steels.

References and Notes

1. D. E. Williams, R. C. Newman, Q. Song, R. G. Kelly, *Nature* **350**, 216–219 (1991).
2. S. Haupt, H.-H. Strehblow, *Corros. Sci.* **37**, 43–54 (1995).
3. I. Betova *et al.*, *Corros. Sci.* **44**, 2675–2697 (2002).
4. J. E. Castle, J. H. Qiu, *J. Electrochem. Soc.* **137**, 2031 (1990).
5. R. C. Newman, *Corros. Sci.* **25**, 331–339 (1985).
6. K. Hashimoto, *Corrosion* **58**, 715–722 (2002).
7. K. Hashimoto, *Appl. Surf. Sci.* **257**, 8141–8150 (2011).
8. C. S. Kiminami *et al.*, *J. Non-Cryst. Solids* **356**, 2651–2657 (2010).
9. M. D. Archer, C. C. Corke, B. H. Harji, *Electrochim. Acta* **32**, 13–26 (1987).
10. J. Schroers, *Adv. Mater.* **22**, 1566–1597 (2010).
11. A. Inoue, *Acta Mater.* **48**, 279–306 (2000).
12. A. L. Greer, *Science* **267**, 1947–1953 (1995).
13. C. J. Byrne, M. Eldrup, *Science* **321**, 502–503 (2008).
14. K. E. Heusler, *Corros. Sci.* **39**, 1177–1191 (1997).
15. J. R. Scully, A. Gebert, J. H. Payer, *J. Mater. Res.* **22**, 302–313 (2007).
16. K. Hono, D. H. Ping, *Mater. Charact.* **44**, 203–217 (2000).
17. G. Okamoto, *Corros. Sci.* **13**, 471–489 (1973).
18. P. Marcus, V. Maurice, H.-H. Strehblow, *Corros. Sci.* **50**, 2698–2704 (2008).
19. M. P. Ryan, D. E. Williams, R. J. Chater, B. M. Hutton, D. S. McPhail, *Nature* **415**, 770–774 (2002).
20. Q. Meng, G. S. Frankel, H. O. Colijn, S. H. Goss, *Nature* **424**, 389–390 (2003).
21. C. Punckt *et al.*, *Science* **305**, 1133–1136 (2004).
22. V. Ponnambalam, S. J. Poon, G. J. Shiflet, *J. Mater. Res.* **19**, 1320–1323 (2004).
23. T. F. Kelly, M. K. Miller, *Rev. Sci. Instrum.* **78**, 031101 (2007).
24. S. O. Klemm, J. C. Schauer, B. Schuhmacher, A. W. Hassel, *Electrochim. Acta* **56**, 4315–4321 (2011).
25. H. M. Ha, J. R. Miller, J. H. Payer, *J. Electrochem. Soc.* **156**, C246 (2009).
26. S. Pang, T. Zhang, K. Asami, A. Inoue, *Mater. Trans.* **43**, 2137–2142 (2002).
27. S. O. Klemm, A. A. Topalov, C. A. Laska, K. J. J. Mayrhofer, *Electrochem. Commun.* **13**, 1533–1535 (2011).
28. K. Ogle, M. Mokaddem, P. Volovitch, *Electrochim. Acta* **55**, 913–921 (2010).
29. N. Homazava, A. Ulrich, U. Krähenbühl, *Spectrochim. Acta, B At. Spectrosc.* **63**, 777–783 (2008).
30. V. Maurice, W. P. Yang, P. Marcus, *J. Electrochem. Soc.* **145**, 909 (1998).
31. A. Pardo *et al.*, *Acta Mater.* **55**, 2239–2251 (2007).
32. S. Fujimoto *et al.*, *Corros. Sci.* **35**, 51–55 (1993).

Geometric Frustration of Icosahedron in Metallic Glasses

A. Hirata,[1] L. J. Kang,[1] T. Fujita,[1] B. Klumov,[2] K. Matsue,[3] M. Kotani,[1,3] A. R. Yavari,[4,1] M. W. Chen[1,5]*

Icosahedral order has been suggested as the prevalent atomic motif of supercooled liquids and metallic glasses for more than half a century, because the icosahedron is highly close-packed but is difficult to grow, owing to structure frustration and the lack of translational periodicity. By means of angstrom-beam electron diffraction of single icosahedra, we report experimental observation of local icosahedral order in metallic glasses. All the detected icosahedra were found to be distorted with partially face-centered cubic symmetry, presenting compelling evidence on geometric frustration of local icosahedral order in metallic glasses.

Determining atomic structure of amorphous materials has been a long-standing problem, because the lack of long-range translational and rotational symmetry renders it experimentally inaccessible by conventional diffraction methodologies. More than half a century ago, Frank proposed that the icosahedron is the most favorable local order in monatomic metallic liquids (*1*), successfully explaining the feasibility of achieving undercooling to below the melting points. Metallic glasses can often be formed from liquid alloys near eutectic compositions and, in accordance with Frank's proposal, binary liquid eutectic compositions can be generated by introducing icosahedral clusters (*2*). Icosahedral order

is thus the most generally accepted description of atomic structures of metallic liquids and glasses (*3*–*14*). From a geometrical viewpoint, icosahedra cannot fill the entire three-dimensional (3D) space, even in disordered systems, without distortion where icosahedral rotational symmetry is partially broken (*15*–*17*). Therefore, the locally preferred icosahedra may not be perfectly consistent with the globally stabilized structure, leading to the theoretical predictions of geometrical frustration of icosahedron (*16*–*19*). Although a number of neutron and x-ray scattering experiments have been performed to elucidate icosahedral order in metallic liquids and glasses (*18*, *20*–*22*), only average structural information can be acquired from 1D diffraction profiles generated by the statistical distribution of coexisting polyhedra with various geometrical distortions in real materials. The direct observation of local icosahedral order is still missing. Consequently, the structure features of local icosahedral order and their correlation with the long-range disorder in glasses and liquids are largely unknown. To overcome the experimental difficulty in detecting local atomic configurations in amorphous materials, we recently developed an angstrom-beam

electron diffraction (ABED) method to probe local atomic structure using a ~0.4-nm electron beam (*23*). We use the ABED technique to characterize local icosahedral order in a representative $Zr_{80}Pt_{20}$ metallic glass in which the presence of a large fraction of icosahedra has been predicted by computational simulations (*24*, *25*) and this study (fig. S1).

The amorphous structure of the $Zr_{80}Pt_{20}$ metallic glass was confirmed by spherical aberration–corrected high-resolution transmission electron microscopy (TEM), together with selected-area electron diffraction (fig. S2). To obtain local structural information, we employed the ABED technique with a beam diameter of 0.36 nm (full width at half maximum) to characterize a thin foil of the glass (Fig. 1A). To guide the ABED study, we simulated the characteristic ABED patterns of an ideal icosahedron along five-, three-, and twofold directions (Fig. 1B). A large number of ABED patterns were acquired from the thin edge of the TEM foil. When the specimen thickness is thin enough (~3 to 5 nm), individual polyhedra with an appropriate on-axis orientation can be frequently detected by ABED. However, from these measurements we cannot find any ABED pattern that is completely consistent with the simulated icosahedron patterns shown in Fig. 1B. Instead, the acquired ABED patterns only partially match those of the five-, three-, and twofold orientations (Fig. 1C). This is probably due to distorted icosahedra in which icosahedral order is only partially preserved. We thus simulated five-, three-, and twofold ABED patterns of a typical <0 0 12 0> icosahedron taken from the molecular dynamics (MD) model of the metallic glass (fig. S1B). All icosahedra in the MD model are actually distorted from the ideal icosahedron, in agreement with theoretical and computational predictions (*17*–*19*, *24*, *25*). Figure 1C shows the simulated five-, three-, and twofold ABED patterns of the distorted icosahedron.

[1]WPI Advanced Institute for Materials Research, Tohoku University, Sendai 980-8577, Japan. [2]Joint Institute for High Temperatures, Russian Academy of Sciences, Moscow 125412, Russia. [3]Mathematical Institute, Tohoku University, Sendai 980-8578, Japan. [4]Euronano, SIMAP-CNRS, Institut National Polytechnique de Grenoble, BP 75, 38402 St. Martin d'Heres Campus, Grenoble, France. [5]State Key Laboratory of Metal Matrix Composites, School of Materials Science and Engineering, Shanghai Jiao Tong University, Shanghai 200030, PR China.

*Corresponding author. E-mail: mwchen@wpi-aimr.tohoku.ac.jp